DOI: 10.13009/EUCASS2023-435
Aerospace Europe Conference 2023 – 10TH EUCASS – 9TH CEAS

ACTiVE – Experimental investigation of the pressure distribution of linear aerospike nozzles with aerodynamic thrust vectoring

Jan Sieder-Katzmann[⋆†], *Martin Propst*[⋆], *Ralf H. Stark* [‡], *Dirk Schneider* [‡], *Stephan General* [‡], *Martin Tajmar*[⋆] *and Christian Bach*[⋆]

[⋆]*Technische Universität Dresden*
Marschnerstrasse 32, 01307 Dresden, Germany
[‡]*DLR Lampoldshausen*
Im Langen Grund, 74239 Hardthausen, Germany
jan.sieder-katzmann@tu-dresden.de · martin.propst@tu-dresden.de
[†]Corresponding author

Abstract

A cold-gas test campaign has been conducted at the DLR's P6.2 test bench in Lampoldshausen to investigate linear aerospike nozzles in interaction with secondary injection thrust vector control (SITVC). Nozzle truncation and injection position are analysed w.r.t. their influence on the nozzle surface and base pressure. While the effects of injection position and truncation on the nozzle surface pressure development are comparable for all geometric variations, their influence on the base pressure appears not to be so easily predictable. Furthermore, the required pressure ratio of the injection flow to the primary flow for a sonic injection is analysed, revealing that experiments with trans-sonic injection have been carried out.

1. Introduction

Aerospike nozzles are well known for their height adaptive capabilities and their additional performance potential compared to classical bell nozzles.[1–3] Engines with aerospike nozzles were in discussion for the replacement of the F-1 engine in the Saturn V rocket (J-2T-250K) and for application in the Space Shuttle Main Engine as well as the Shuttle's successor in the Venture Star project (XRS-2200).[4] However, they have not been put into service by any launch service provider so far. In university projects, like the California Launch Vehicle Education Initiative (CALVEIN)[5] , the Dryden Aerospike Rocket Test[6] and Daedalus Astronautics[7] , the aerospike engine remained an attractive research topic and regained attention with the emergence of new private launch providers. With Firelfy Alpha[8] (at the beginning), RocketStar Space[9] , Ripple Aerospace[10] and most recently Pangea Aerospace[11] , several newcomers announced to use an aerospike engine due to the expected performance advantage. Most recently, the achievement of a long-time stable combustion of an aerospike engine by Pangea Aerospace in 2021[12] increased the confidence of bringing the aerospike engine into application. For thrust vector control (TVC) for aerospike engines, the most promising technological approach in the low and medium thrust range seems to be secondary injection thrust vector control (SITVC).[13] The utilization of SITVC allows to remove the heavy gimbal from the propulsion system and does not require throttling capability of the engine like differential throttling.
To our knowledge, aerospike engines using SITVC have been subject to experimental research and development by mainly two actors: Rocketdyne in the 1960s (report by Silver[14]) and Eilers et al[15–17] at Utah State University in the 2010s. The report by Silver comprised 33 hot-fire tests, in which they studied the effect on thrust vectoring performance on an annular nozzle with a variety of injection positions, secondary mass flows and injection patterns. Within the MUPHyN-project, Eilers et al. investigated SITVC by combining CFD simulations, cold-flow and hot-fire tests. For three different injection positions, they evaluated the performance of side-force generation in terms of side specific impulse for the respective secondary mass flow. Both projects focussed on annular nozzle development with the aim of making the system ready to be used and not on obtaining fundamental research data. They neither focussed on linear nozzles nor a specific measurement of the pressure distribution during SITVC-operation. In recent years, Ferlauto et al. conducted numerical simulations on annular[18] and linear[19] aerospike nozzles with SITVC. Furthermore, they compared the performance potential of SITVC with a system utilizing differential throttling.[20,21]

DOI: 10.13009/EUCASS2023-435

In the frame of the research project ACTiVE at Technische Universität Dresden, we SITVC on linear and annular aerospike nozzles, utilizing numerical analyses and experiments. Numerical simulations[22,23] , accompanied by shallow water experiments[24,25] , have shown the general functionality of SITVC and laid the foundation for this project. In parallel, a profound literature review[13] has indicated that SITVC is a favourable solution to steer rockets and space crafts with aerospike nozzles in general and in case of single chamber engines in particular. However, the accessible data base and technological knowledge on secondary injection for aerospike nozzles is insufficient for an expedient engine development. Hence, it is the aim of this project to improve this insufficient data situation.
In cooperation with the Flows Group of the Space Propulsion Institute in Lampoldshausen (German Aerospace Center, DLR), a test campaign on two-dimensional, linear aerospike nozzles utilizing SITVC was conducted in summer 2019 following a pre-test campaign in December 2018.[26] The latter was successfully conducted in order to verify the functionality of the test specimen itself, identify of any technical issues, as well as to verify the flow visualisation and the surface pressure measurement concepts. The main goal of the 2019 test campaign was to thoroughly investigate the flow phenomena and the pressure distribution on the nozzle surface. An aerospike nozzle test specimen with exchangeable plugs (central nozzle body) was manufactured to meet the specifications of the cold flow test stand P6.2 in Lampoldshausen. A total of four different plugs were tested, which differ in their geometry in terms of truncation and secondary injection location. One plug was manufactured without the injection and is used as reference. The individual geometry of the plugs is consecutively building up with only one modification each. Therefore, the influence of the secondary injection, its location and the truncation of the plug can be evaluated separately.

The general description of the experimental set-up is given in section 2. It summarizes the test bench P6.2 at the Space Propulsion Institute and the sensor equipment for surface pressure measurements including the optical systems for flow visualization. The test specimen is presented as well in terms of design, manufacturing and realization in a dismountable assembly. Special focus lies on the variability of the test specimen through exchangeable plugs with different truncation lengths and positions for the secondary injection (SI). The results of the test campaign from summer 2019 are presented in section 3, which contain the surface pressure measurements on the nozzle flow with active SI. Furthermore, the base pressure measurements are shown in dependency of the nozzle pressure ratio and its influenceablity with secondary injection. A brief discussion and assessment of the results follows in section 4.

2. Experimental set-up

The experimental set up was designed for and has been realized at the cold gas test bench P6.2 at the Space Propulsion Institute of the German Aerospace Center. At the beginning of this section, a brief description of the test bench is given. It is followed by a detailed explanation of the test specimen design procedure. The section is concluded with the realization of the test specimen. This set up description is an updated version, which was part of an earlier publication.[26]

2.1 Cold gas test bench P6.2

The cold flow test facility P6.2 has been implemented at the Space Propulsion Institute in late 1998. It is used for nozzle or diffuser tests at ambient and high altitude conditions using gaseous nitrogen (GN2). The test facility provides up to three gas feeding lines, which can be separately controlled in pressure. The first feeding line is used for the primary main flow expanding into ambient pressure. A second line will be used to feed the secondary injection. Table 1 summarizes of the relevant performance data of the test bench.

The fluidic interface for the test specimen is mounted on a frame. A corrugated metal hose with an inner diameter of 125 mm provides the feeding gas for the main flow. It is connected to a diffuser, followed by a flow straightener and a pressure measurement flange used to obtain the total pressure $p_{0,main}$. The last flow component upstream of the test specimen is the Börger-contraction[30,31] , which compresses the flow uniformly into a square 45 mm × 45 mm cross section.
The second feeding line for the injection flow is realized with a corrugated metal hose with an inner diameter of 6 mm. This hose is connected via a stainless steel elbow with an inner diameter of 8 mm and an adapter to a straight stainless steel tube with an inner diameter of 10 mm. In the latter, after a flow settling length of 50 cm, a Swagelok® T-piece is used to mount a pressure sensor to measure the static injection pressure p_{inj}. 18 cm downstream, another T-piece follows to guide the injection flow through two feeding lines, in order to obtain a symmetric and force free inflow into the test specimen. The mounted test specimen with the feed lines is shown in figure 1.

A second interface is defined for the pressure measurement. Sensor blocks, which hold the Kulite® pressure transducers (types XT-154-190M and HKM-375M) with corresponding pressure ranges (0.1 MPa - 5.0 MPa), are mounted near the test specimen . Steel tubulations from Scanivalve® are glued into these sensor blocks and are directly

DOI: 10.13009/EUCASS2023-435

Table 1: P6.2 Performance data[27–29]

System	Data
Gas supply system	
	GN2 cold gas
	Mass flow per line $\dot{m} \leq 4.2\,\mathrm{kg/s}$
	Total pressure main flow $p_{0,main} \leq 6.0\,\mathrm{MPa}$
	Total pressure injection flow $p_{0,inj} \leq 4.0\,\mathrm{MPa}$
	Gas supply: ≈ 989 standard m^3
	Test time $> 120\,\mathrm{s}$ (full flow)
Measurement and control system	
	Low frequency (LF) data akquisition system[a]
	Provides up to 64 channels at 1 kHz
	50x Anti-aliasing filter for LF
	Data capacity per test up to 4 GB

[a] 8-16 high frequency channels (up to 100 kHz) available

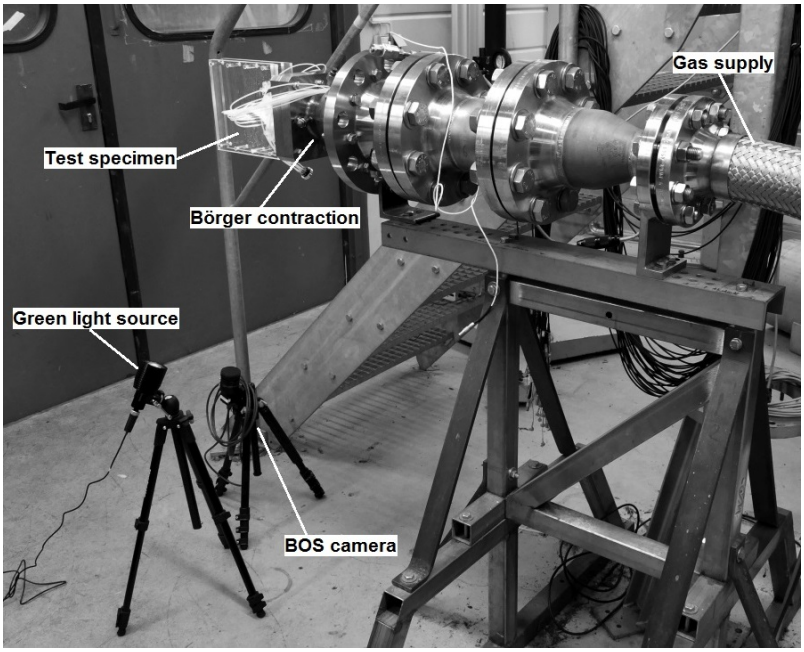

(a) Plug 1 nozzle with primary feed line and BOS set-up

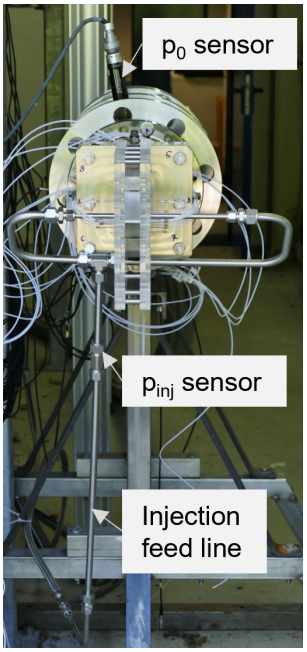

(b) Plug 3 nozzle with injection feed line and and pressure sensors

Figure 1: Mounted test specimens and gas supply lines

connected to the test specimen via Teflon tubes, which have a diameter of 1.6 mm.

In addition to the surface pressure measurements, flow visualization is a key aspect of this campaign. Two different flow visualization systems are used. A Z-Schlieren set-up, using a Photron® FASTCAM 1024 PCI high speed camera, depicts the flow perpendicular to the two-dimensional nozzle plane (see fig. 2). And a BOS-system captures the flow lateral from within this plane (see fig. 1). The latter consists of a monochromatic Blackfly S Mono 5.0 MP USB3 Vision camera with a green band filter (MIDOPT FIL BP525/37.5 525 nm) and a green light spot for a homogeneous illumination. Both systems catch changes in brightness where light is deflected due to a refractive index gradient, e.g. caused by a density gradient. Hence, they are highly decent to capture shocks and other phenomena expected in a supersonic flow.

DOI: 10.13009/EUCASS2023-435

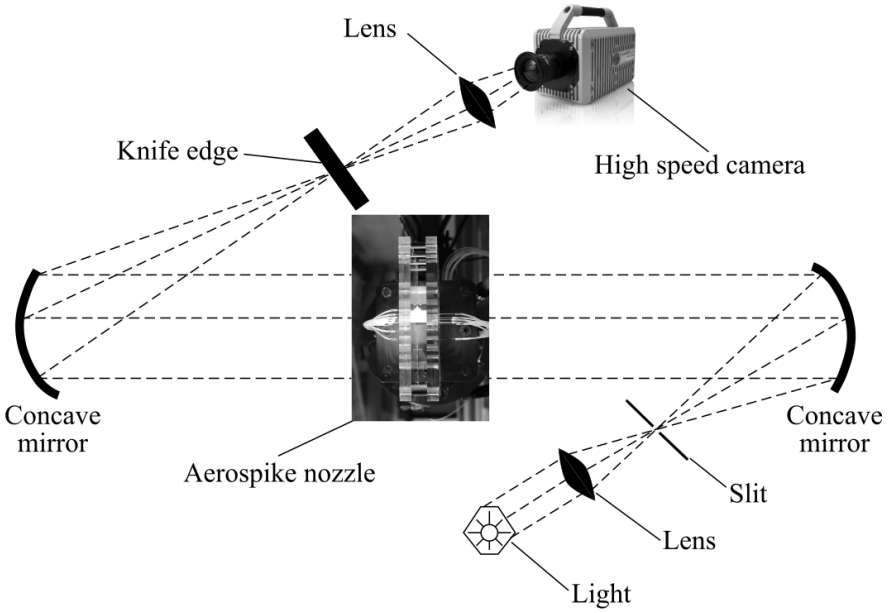

Figure 2: Schematic of the Z-Schlieren set-up

2.2 Test specimen design

The general design of the test specimen and in particular the supersonic part of the nozzle is derived to fit best the test bench capabilities. As shown in table1, the highest realizable mass flow is $\dot{m}_{max} = 4.2\,\mathrm{kg/s}$ and a maximum total pressure of $p_{0,max} = 6\,\mathrm{MPa}$. Hence, he maximum throat area is derived with $A_{t,max} \leq 300\,\mathrm{mm}^2$ using $p_{0,max}$ using the gas properties for nitrogen at room temperature.

The normalized nozzle contour has been obtained with an adaptation of the FORTRAN program of C. C. Lee[32] for linear aerospike nozzles. Using the Prandtl-Meyer expansion, for each characteristic (straight Mach line) originating at the outer lip of the nozzle throat, the corresponding flow area necessary is calculated for a constant mass flow. For the derivation of a specific contour, some input parameters are necessary. Besides the gas properties, the design pressure ratio $NPR_d = (p_0/p_e)$ between total pressure p_0 and nozzle exit pressure p_e is needed. Since the nozzle will expand into ambient pressure $\approx 100\,\mathrm{kPa}$, the nozzle exit pressure is set to this value. Hence, $NPR_{d,max}$ is limited to ≈ 60 considering $p_{0,max}$. With the goal of testing all flow states from over-expanded, adapted and under-expanded, a slightly lower design pressure ratio of $NPR_d = 45$ has been chosen. Furthermore, a trade-off between nozzle width w_n and nozzle radius R_E (technically the nozzle height) was conducted, which is described in more detail in the preceding publication.[26] Table 2 summarized the finalized input parameters for the nozzle dimensioning and key results are displayed.

Figure 3 shows the final nozzle contour indicating the truncations 34.5 % and 64.5 % and the secondary injection sites at 15 % and 40 % w.r.t. the full isentropic length. The truncations have been chosen such that they represent a rather larger and a rather small truncation rate, which can both be manufactured and drilled into to take in a pressure steel tubulation. Aiming for a rather downstream injection w.r.t. the nozzle, the two injection locations were chosen such that they are close to the respective nozzle truncation but still allow one or two pressure measurement locations downstream of the injection.

2.3 Realization of the test specimen

The test specimen is designed and manufactured as a screwed assembly. The assembly consists of the combustion chamber and four different plugs and two acrylic side plates each to ensure a two-dimensional flow. All parts are connected by stainless steel screw as shown in figure 4.

The combustion chamber is made of stainless steel and its components are brazed together to ensure leak tightness. This sub-component serves on one hand as the mechanical interface to the test bench with its flange and realizes on the other the gas flow distribution by adapting the flow cross section to a rectangle of $20\,\mathrm{mm} \times 45\,\mathrm{mm}$. This cross section is continuously decreased towards the nozzle throat.

DOI: 10.13009/EUCASS2023-435

Table 2: Input values and outputs from nozzle design program[26]

Parameter	Value
Input	
Design pressure ratio NPR_d	45
Isentropic exponent κ	1.4
Nozzle width w_n	20 mm
Nozzle radius R_E	36 mm
Output	
Area ratio $\epsilon = A_e/A_t$	4.82
Throat area A_t	298.7 mm^2
Ideal thrust coefficient c_F	1.475

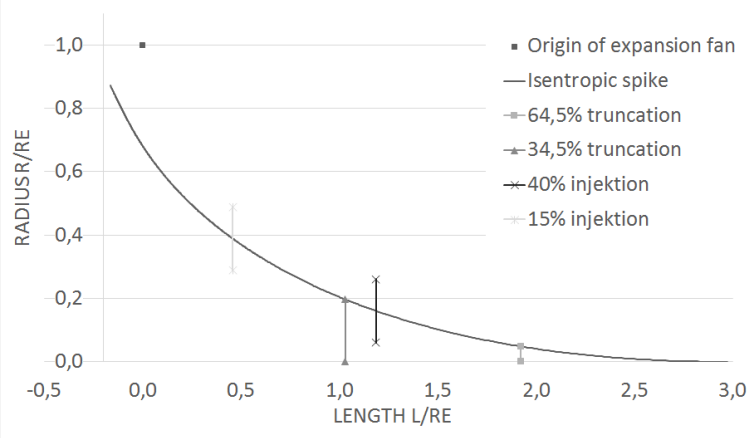

Figure 3: Normalized isentropic nozzle contour with marks for truncations and secondary injection positions[26]

A t-slot clamp connects the four different plugs mechanically to the combustion chamber. Each of the plugs is made of aluminium and varies just in one geometric parameter from its number predecessor, as shown in figure 5. Plug 1 is the reference plug with the greater length and no secondary injection. Up-following, plug 2 has the same length and the downstream secondary injection site. The plug with the same length and an upstream injection site is called plug 3. At last, plug 4 shares the injection position with plug 3, but is more truncated. Each injection is fed by a second gas supply line through a steel pipe with 8 mm outer diameter and 1 mm wall thickness.

The acrylic plates not only ensure the two dimensional flow, but separate also the nozzle flow from the ambient. Furthermore, in case of the plugs 2 - 4 with secondary injection, the acrylic plates separate the two nozzle flows from each other and prevent a flow around the plug due to the different pressure distribution. Eight 8 mm bolts are used to stiffen the acrylic plates and to ensure a constant spacing in-between. They are mounted with some distance from the nozzle so that the nozzle flow remains unaffected.

For the pressure measurement, each plug is equipped with a number of pressure measurement holes, which share all the same center-lined position on each plug. These holes have a diameter of 0.5 mm and are drilled perpendicular to the local surface. On the plug side with the secondary injection, the measurement holes are spaced with a axial distance of $\approx$ 7 mm, where the density is doubled around injection positions (name suffix A). The locations of the secondary injection sites coincide with pressure measurement holes of other plugs.
Furthermore, in order to ensure comparable pressure measurements between all plugs, two holes are duplicated on the opposite site of the injection, indicated with *u*. Three additional measuring holes are added with 5 mm distance to one wall, that are indicated with *w*. They are used to evaluate the effects of the wall shear layer development due to the acrylic side plates on the pressure measurements.
Each plug is equipped with two measurement holes at the plug base, one in the middle and the other near the wall. The wider base of plug 4 even allowed two additional pressure measurement holes in the center line with a lateral displacement. This allows the analysis, if the secondary injection has an influence on the symmetry of pressure distribution of the nozzle base. All pressure measurement locations are summarized in table 3.

DOI: 10.13009/EUCASS2023-435

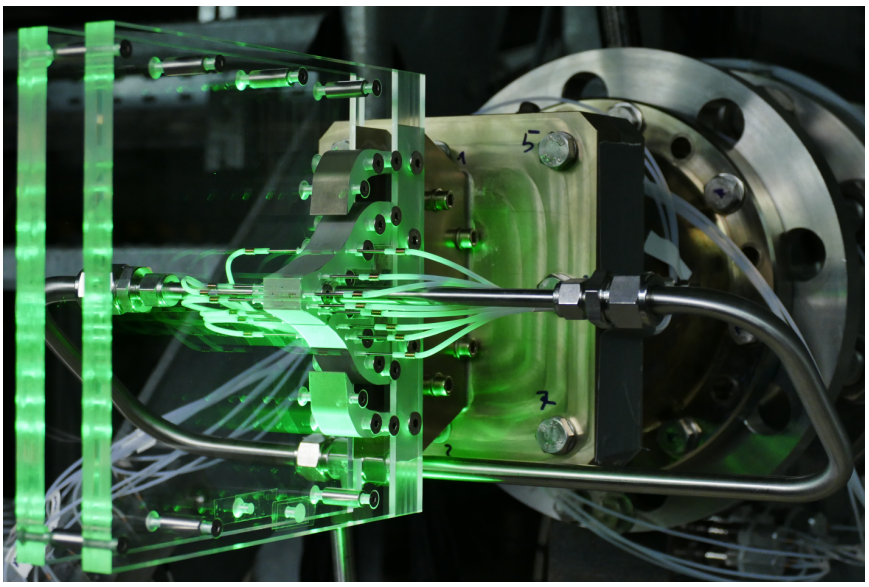

Figure 4: Set up specimen with Plug 4 on the test bench

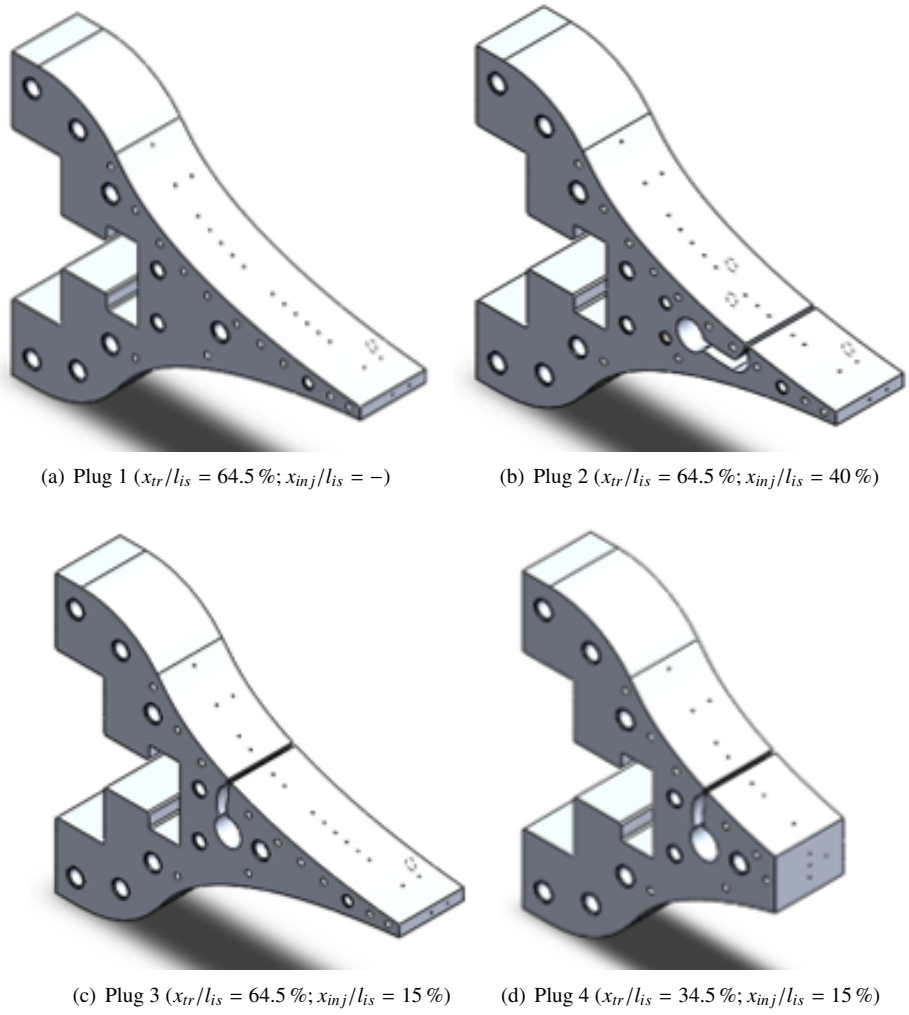

(a) Plug 1 ($x_{tr}/l_{is} = 64.5\,\%; x_{inj}/l_{is} = -$)

(b) Plug 2 ($x_{tr}/l_{is} = 64.5\,\%; x_{inj}/l_{is} = 40\,\%$)

(c) Plug 3 ($x_{tr}/l_{is} = 64.5\,\%; x_{inj}/l_{is} = 15\,\%$)

(d) Plug 4 ($x_{tr}/l_{is} = 34.5\,\%; x_{inj}/l_{is} = 15\,\%$)

Figure 5: Exchangeable plugs of the test specimen with their relative truncation x_{tr}/l_{is} and injection position x_{inj}/l_{is}

DOI: 10.13009/EUCASS2023-435

Table 3: Measuring hole locations on the plugs[26]

	Position #	**Axial position [mm]**
Plugs 1-4	01	-4.5
	02 (u, w, uw)	2.5
	03	9.5
	03A	13.0
	04	16.5
	04A	20.0
	05 (u)	23.5
	06	32.3
Plugs 1-3	06A	35.8
	07	39.3
	07A	42.8
	08	46.3
	08A	49.8
	10 (w)	60.3
	Base (w)	69.1
Plug 4	Base (w)	36.9
		(lateral position 0.0)
	Base (o, u)	36.9
		(lateral position ±3)
name affixes:	o: additional hole on injection side	
	u: additional hole on opposite side	
	w: additional hole near the wall	
	uw: additional combination of u and w	

3. Results

After the description of the test set-up in the last section, a presentation of the measurement results follows here. At first, an overview is given of the applied test sequence for the different plugs. Subsequently the surface pressure measurements are are analysed for the reference plug and the ones with secondary injection. In conclusion of this section, the measurements of the base pressure are presented and analysed w.r.t. its influenceability by the secondary injection .

3.1 Test sequence

Before the test results can be presented, the test sequences that were used during the test campaign are described. In general, the maximum feeding pressure of the primary and injection flow are set to the maximum desired value (in this case: $p_0 = 6.8\,\text{MPa}$ and $p_{inj} = 3.8\,\text{MPa}$), while control valves are driven to reach specific total pressure limits. Figure 6 shows the applied test sequences for the reference nozzle Plug 1 and Plugs 2 - 4 in case of active injection.
The both have in common a similar main flow total pressure p_0 profile, which begins with a ramp up transition up to the highest level. After reaching the first plateau, two further steady states follow at lower pressure levels. Each of the plateaus lasted 10 seconds. Thereafter, the main flow valve is closed and the test ends.

In case of secondary injection, the first plateau consists of two phases, again 10 seconds each, for which the first one has no active injection but the second. 50 seconds after the beginning of the test, the control valve for the injection flow is fully opened and remains so until the end of the test and the pressure regulator remains unchanged. From Figure 6 become two sensor patterns in mind that are not directly intuitive: At first, during the test time in between 5 and 45 seconds, the pressure reading for p_{inj} is raising. This is due to the filling of the cavity between the control valve and the injection site. Hence, the injection site acts like a pressure measurement port with a large time constant. The second pattern is obvious after about 105 seconds, where p_{inj} decreases significantly with the reduction of the main flow total pressure. Therefore, there seems to be a coupling between both pressures, which is addressed further in section 4.2.

DOI: 10.13009/EUCASS2023-435

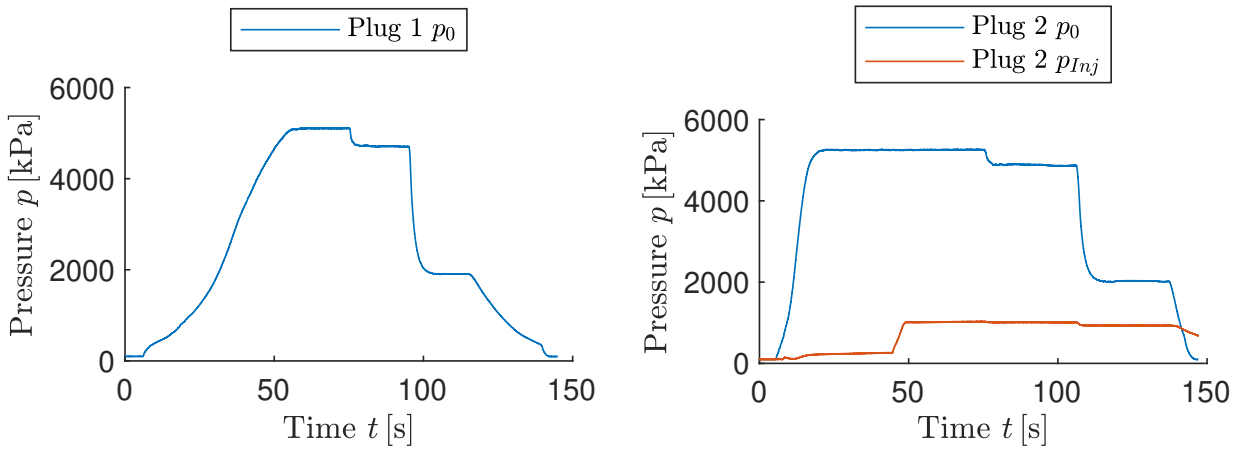

(a) Test sequence without secondary injection (Plug 1)

(b) Test sequence with secondary injection (Plugs 2 - 4)

Figure 6: Test sequences used in the presented test campaign

3.2 Plug surface pressure

Reference nozzle - Plug 1

After the test sequences have been defined, the measurement results are presented. At first, the full isentropic pressure distribution of the reference plug 1 is shown in Figure 7. It can be seen, that for the underexpanded condition of $NPR = 51.60$ and $NPR = 47.63$ the normalized pressure ratio p/p_0 decrease continuously in a nearly ideal isentropic manner and are almost identical. This behaviour is due to the fact that, above the design pressure ratio (NPR_d), the pressure adaptation of the nozzle is solely realized beyond the nozzle surface and therefore does not affect the normalized pressure distribution on the plug surface. A deviation from that behaviour can be noticed in the most downwind measurement positions for the overexpanded flow state of $NPR = 19.28$. The normalized pressure ratio suddenly increases downstream of the nozzle position $x/R_E = 1.3$. This can be explained with the recompression of the flow that occurs, when the pressure of the flow is expanded below p_{amb}. This recompression occurs in form of a shock which interacts with the nozzle surface and can be identified in the corresponding Schlieren image in Figure 8.

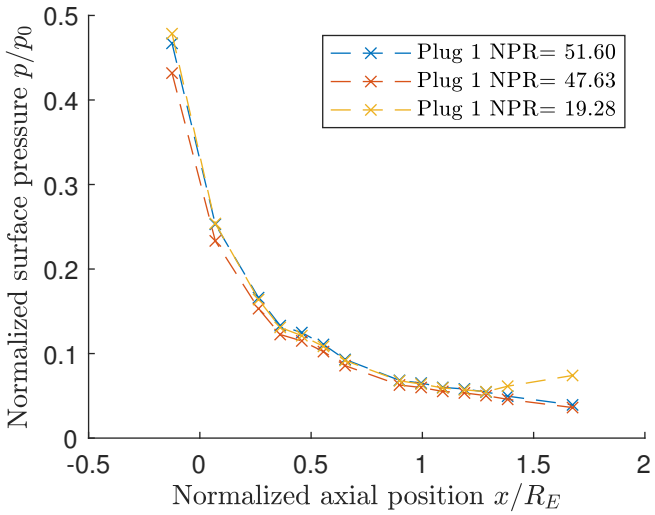

Figure 7: Pressure ratio on Plug 1 at different NPRs

Nozzles with secondary injection - Plugs 2 - 4

For the analysis of the surface pressure with actived SITVC, the two flow states with an the $NPR \approx 20$ and $NPR \approx 52$ are used, since the two underexpanded ones are very similar. Figure 9 on the left shows the measured pressure ratio

DOI: 10.13009/EUCASS2023-435

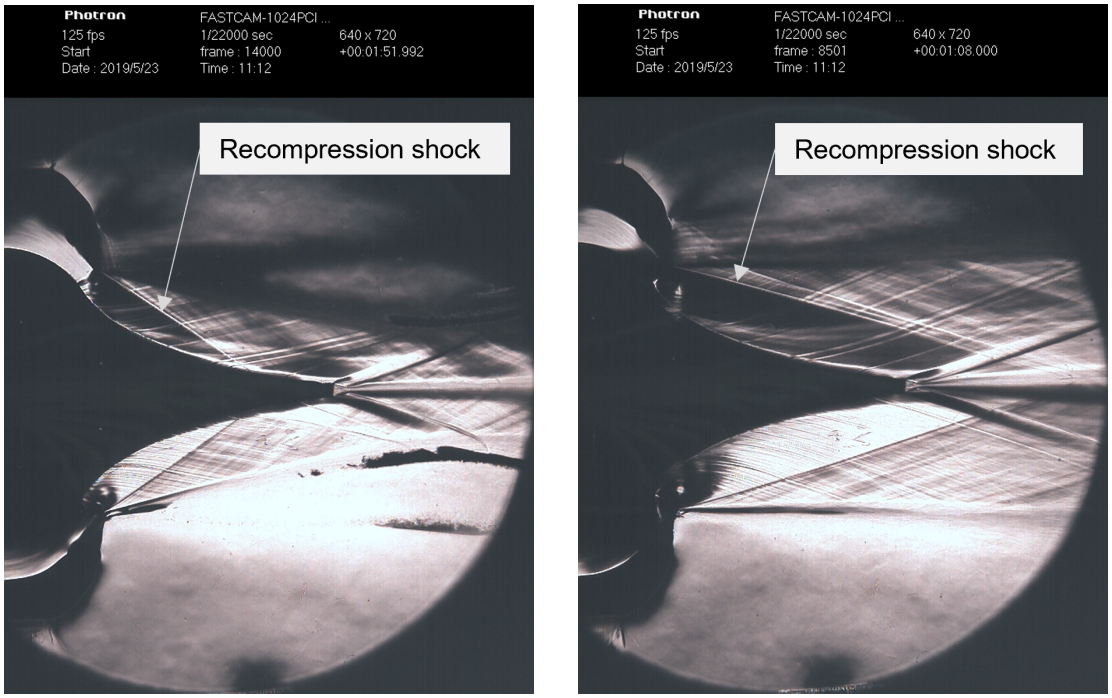

(a) Overexpanded flow ($NPR \approx 20$)

(b) Underexpanded flow ($NPR \approx 52$)

Figure 8: Schlieren pictures of Plug 1 at different main flow conditions

for the Plugs 2 to 4 in the mentioned flow states. For the overexpanded flow state ($NPR \approx 20$) a distinct increase in the pressure is apparent upstream of the respective injection position for each plug. This high pressure region is very similar for the identical injection positions of Plug 3 and 4. For Plug 2 with the downstream injection position, the pressure increase is more extended and has a flatter gradient. Downstream of the injection, a pressure decrease is measured for all three Plugs, which is highest directly at the injection and flattens out further downstream. Especially for Plug 3, this zone of decreased pressure appears to be regionally confined. Again, this region of decreased pressure is for Plugs 3 and 4 very similar, while for the downstream injection of Plug 2 a different behaviour is noticeable. Here, a slight increase in pressure w.r.t. the measurement of Plug 3 can be observed, which indicates a interaction of the recompression shock with the injection slots situated in the more upstream or downstream position.

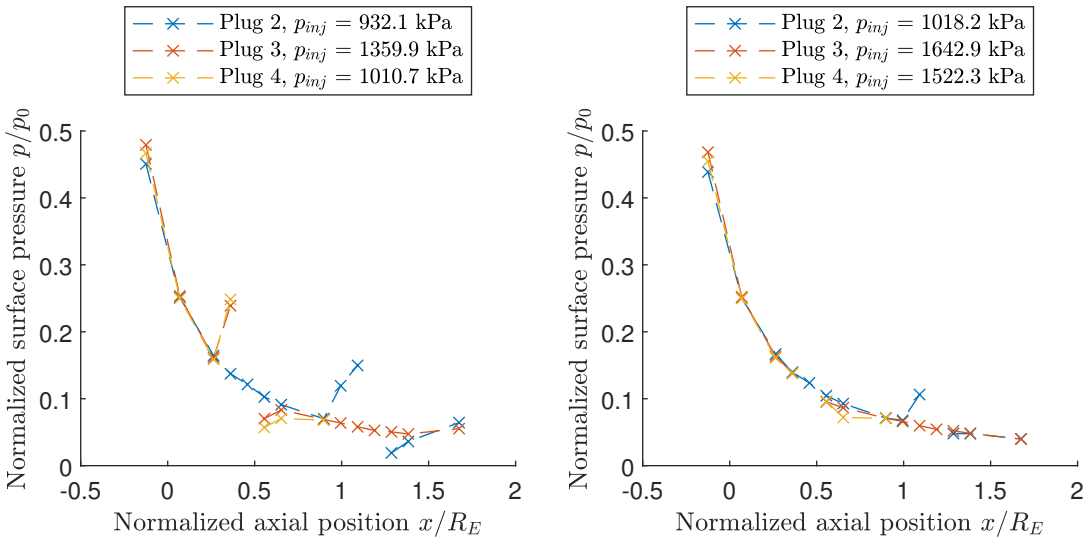

(a) Overexpanded flow ($NPR \approx 20$)

(b) Underexpanded flow ($NPR \approx 52$)

Figure 9: Surface pressure of Plugs 2-4 at different main flow conditions

DOI: 10.13009/EUCASS2023-435

For the underexpanded flow state of $NPR \approx 52$, the influence of the secondary injection on the primary flow pressure distribution is significantly less prominent, as shown in Figure 9 on the right side. The high pressure region in front of the upstream injection (Plugs 3 and 4) can not be measured with the test specimens. Only the downstream injection on Plug 2 shows an increased pressure upstream of the injection site. On the other hand, the low pressure regions downstream of the injection are clearly visible for the upstream injection ($x_{inj}/l_{is} = 15.4\,\%$), while no significant pressure decrease is noticeable for the downstream injection at $x_{inj}/l_{is} = 40.4\,\%$.
At last, it has to be pointed out that the measured static injection pressure diverges for both flow states ($NPR = 20$ / $NPR = 52$) significantly, see legend of Figure 9 - even though the pressure regulator setting and the control valve opening have not been changed.

3.3 Base pressure measurements

Base pressure without secondary injection

During the first transient phases of the test sequence with increasing total pressure p_0, the base pressure ratio p_{base}/p_0 with inactive secondary injection is evaluated w.r.t. the nozzle pressure ratio. The correlation of p_{base}/p_0 and the NPR is shown in Figure 10 for different plugs and measurement positions in a NPR-range between 1 and 60. It becomes obvious that the two variations of truncation $x_{tr}/l_{is} = 64.5\%$ for Plugs 1-3 and $x_{tr}/l_{is} = 34.5\%$ for Plug 4 have a similar but clearly distinguishable behaviour. At nozzle pressure ratios until approximately $NPR = 3$, the base pressure ratio decreases continuously for all plugs and remains below the ambient pressure, followed by a series of sharp oscillations until $NPR \approx 6$. Beyond that, the p_{base}/p_0-behaviour starts to differ between Plugs 1-3 and Plug 4. The base pressure ratio for Plugs 1-3 (longer plug) passes through a local minimum followed by a local maximum at $NPR = 12$. In the region of this local maximum, the base pressure exceeds the ambient pressure. At NPRs above that maximum, the base pressure ratio falls below the ambient pressure value and decreases monotonously until $NPR \approx 32$, above which it becomes constant. For the shorter Plug 4, the local maximum in the base pressure ratio appears already at $NPR \approx 8$. This maximum is again above the ambient pressure ratio p_{amb}/p_0 and is followed by a monotonous p_{base}/p_0-decrease. The base pressure ratio becomes constant for $NPR > 24$, which indicates, that the base pressure becomes solely dependent on the total pressure p_0, respectively independent from the ambient pressure p_{amb}. This behaviour is widely known in literature as 'wake closing'. At $NPRs$ above ≈ 45 the base pressure exceeds again the ambient pressure and therefore causes a net gain in thrust for the base area.

Impact of secondary injection on the base pressure

The two transients during the main flow pressure reduction are used for investigating the impact of the secondary injection flow on the base pressure. Figure 11 shows base pressure ratios for the central base pressure measuring points with and without injection flow for Plugs 2 - 4. For the longer plugs 2 and 3, a minimal increase in base pressure can be observed for the injection case w.r.t. the non-injection case. But the effects in the proximity of the wake transition are different. For Plug 2, the p_{Base} reading in the injection case follows very close to the non-injection case, with a small offset.
In case of Plug 3, the base pressure with active injection behaves differently. On one hand, the wake closing transition is slightly moved to a lower NPR from ≈ 32 to ≈ 28. On the other hand for $NPRs$ below the transition phase, the base pressure is slightly reduced w.r.t. to the non-injection case except for a narrow range of intersection around $NPR = 15$. For shorter Plug 4 no change in the base pressure is noticeable caused by the secondary injection. P_{Base}/p_0 remains the same for the closed wake condition of the non-injection case. However, the wake closing transition is substantially shifted to a lower NPR of ≈ 20 for the injection case.

It can be summarized for the injection position: In case of the more upstream injection (Plugs 3 and 4), an active injection shifts the wake closing transition to a lower NPR. But the injection does not seem to have any influence on the transition in case of the downstream injection (Plug 2). Furthermore w.r.t. truncation, the base pressure level is slightly increased for the plugs with less truncation (Plugs 2 and 3), while the base pressure seems to be unaffected by the injection in case of the higher truncation (Plug 4).

Flow symmetry analysis of Plug 4

At last, a potential flow asymmetry due to the asymmetric secondary injection shall be investigated on Plug 4. For this case, Figure 12 shows the pressure ratio for the three centre-lined measurement holes for the cases of inactive and active injection. As discussed above, the injection seems to have no effect on the general pressure level at the base in closed wake mode and shifts the wake closure to a smaller NPR. Furthermore, during active injection, no significant difference between the pressure measurement closer to the injection side $PBaseO$ can be observed w.r.t.

DOI: 10.13009/EUCASS2023-435

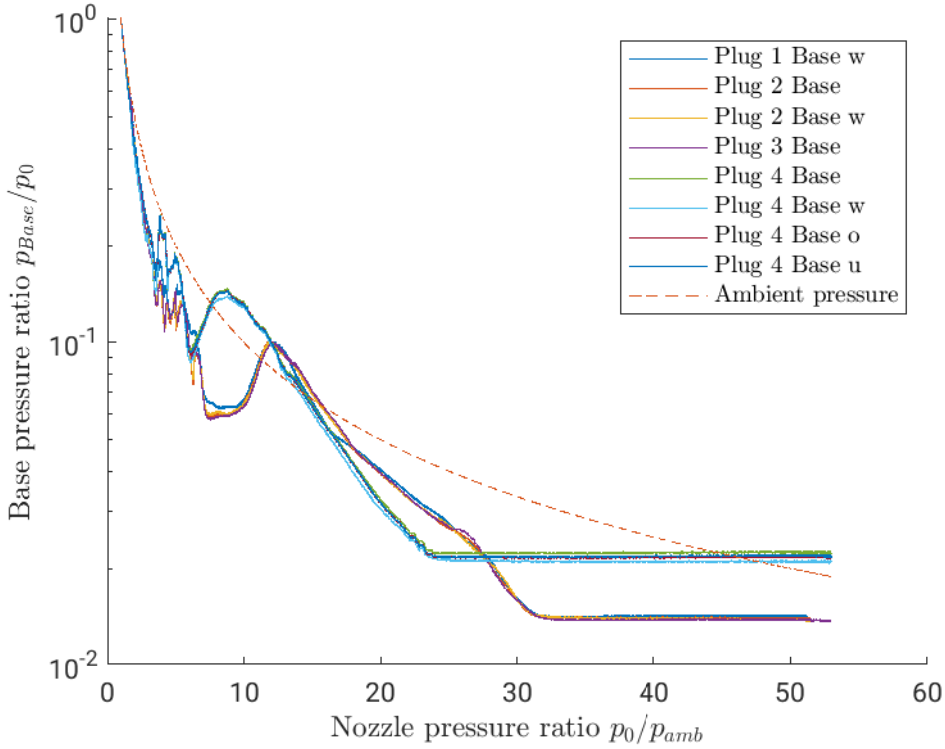

Figure 10: wake closure, base pressure ratio over NPR

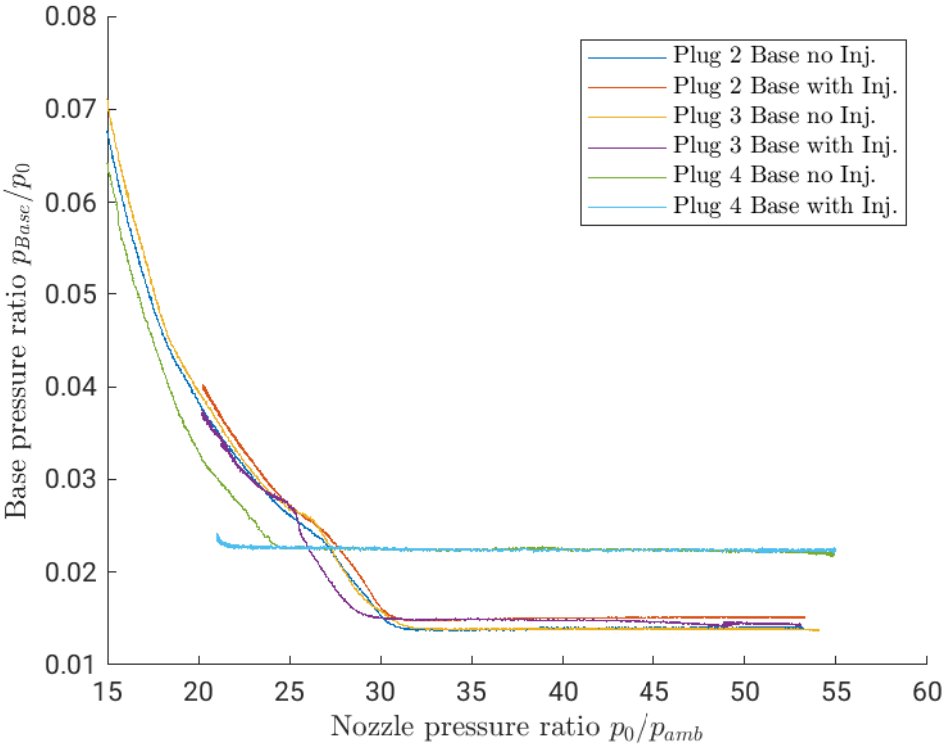

Figure 11: base pressure change at different NPR due to injection

DOI: 10.13009/EUCASS2023-435

the opposing side *PBaseU*. Hence, no wake asymmetry could be measured with this set-up and flow conditions. The only significant deviation observable are the lower pressure at the base center nozzle pressure ratio of $NPR \approx 4$, where the center measurement is lower than the non-axial ones (BaseO and BaseU). This could be caused by the different distances of the measurement holes from the suction effect of the primary flow.

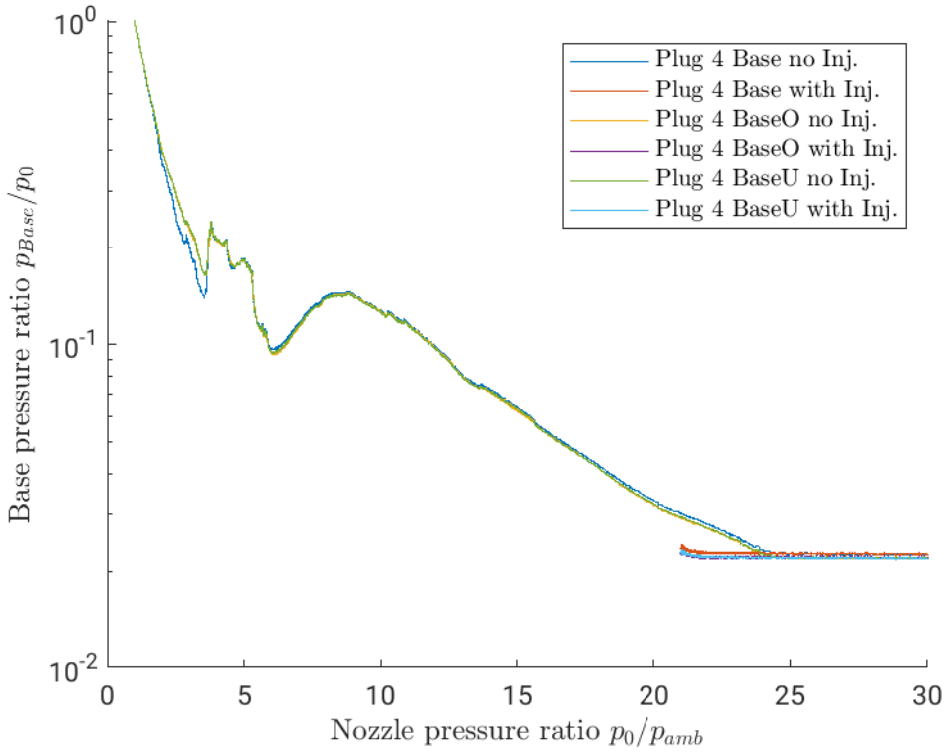

Figure 12: base pressure Plug 4 change at different NPR due to injection

4. Discussion

After the description of the test results, they are briefly discussed and analysed. At first, they are put into context with the corresponding CFD simulations conducted at our institute. Subsequently, a follow-up test campaign is briefly described and evaluated to further analyse the reason for the variations of the injection pressure and verify the assumption of a potential sub-sonic injection flow.

4.1 Comparison with numerical simulations

Already in 2021, Propst et al.[33] have published a flow study using CFD on the here presented test campaign. Exemplary, Figure 13 shows a comparison between the static pressure distribution on the plug surface derived from CFD and the corresponding experimental results. The herein investigated experimental conditions are those as described in section 3.2 and shown in Figure 9. It can be seen, that CFD and experiment are in very good agreement. Hence, the experimental results can serve to validate the numerical flow simulations, which themselves can be used for a deeper flow investigation beyond the limitations of the experiment in terms of pressure measurement and flow visualization limitations.

4.2 Injection velocity

As already mentioned in section 3.1, p_{inj} was changing proportional to the total pressure p_0 of the main flow during an experimental run - despite the fact, that the pressure setting in the regulator and the control valve setting were unchanged. Hence, a coupling of both pressures p_0 and p_{inj} was assumed, which would mean that the injection was

DOI: 10.13009/EUCASS2023-435

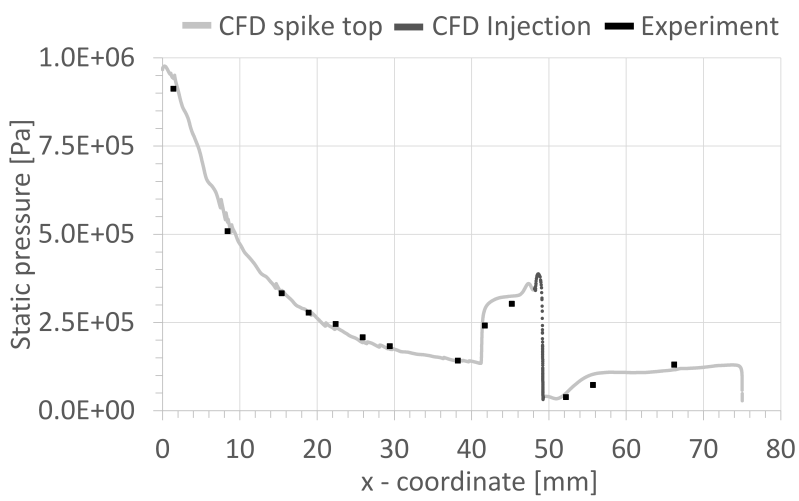

Figure 13: Comparison Measurement vs. CFD[33]

sub-sonic instead of sonic.

In order to verify this assumption, this test campaign has been repeated in the vacuum wind tunnel test bench[34,35] at Technische Universität Dresden with sub-scale nozzle models. These sub-scale nozzles were downsized in the throat area by a factor of 5 and in terms of pressure by factor of 10 to fit the test bench capabilities. With this set-up, a series of measurements were conducted for the two flow states overexpanded ($NPR = 20$) and underexpanded ($NPR = 52$) of the primary flow. The injection pressure p_{inj} has been varied widely to catch the pressure ratios p_{inj}/p_0 experienced in the original campaign - and beyond. With the measured mass flows, the mass flow ratio $MFR = \dot{m}^+_{inj}/\dot{m}^-_{inj}$ is calculated based on the injection mass flow with active $\dot{m}^+_{inj}$ and deactivated $\dot{m}^-_{inj}$ primary flow at a certain injection pressure p_{inj}. The reasoning for this MFR-investigation is that without a primary flow, the injection flow is always sonic due to a pressure ratio w.r.t. ambience $p_{inj}/p_{amb} \gg 2$. Hence, if $MFR \leq 1$, the mass flow is not only depending on p_{inj} but also at the exit conditions for the injection implied by the primary flow, causing a sub-sonic flow.

The obtained MFR-pressure ratio-correlations are summarized in Figure 14 for the nozzle and primary flow state individual measurements. Furthermore, the presented MFR-pressure ratio-correlations for the flow states investigated in section 3 are marked.
In general, it can be seen from this figure, that there are three different ranges in the diagrams. At very low p_{inj}/p_0, the MFR is a linear increasing with the pressure ratio. Beyond a certain pressure ratio, which correlates with the injection position (Plug 2 $p_{inj}/p_0 >\sim 0.4$ and Plugs 3 and 4: $p_{inj}/p_0 >\sim 0.6$), the MFR becomes unity. In-between these two straight lines exists a curved transition zone.

It is obvious from Figure 14 that in the underexpanded primary flow state ($NPR = 52$) $MFR < 1$ for all three Plugs, which means that the injection was sub-sonic. For the underexpanded primary flow state ($NPR = 20$) it is a little bit different: For Plug 2 with the downstream injection, the p_{inj}/p_0 is high enough to ensure a sonic injection. The pressure ratio for Plug 3 is very close to the critical value needed for a sonic injection and seems to be just barely above the threshold to realize a sonic injection. The injection flow state on Plug 4 on the other hand is below the threshold and in the transition range close to a full sonic injection.
In consequence it can be concluded, that in most of the investigated flow states a sub-sonic injection was achieved. Only in a few experimental phases, especially during an overexpanded primary flow state, a sonic injection could be achieved. Hence, it is critical to realize a pressure ratio p_{inj}/p_0, which is above the threshold in order to ensure a sonic injection. In the presented test campaign, it is assumed, that especially the comparably low diameter of the metal hose in the injection feeding line caused a to high pressure loss to achieve the required pressure ratio for sonic injection in all experimental phases.

However, these results are not only relevant in terms of knowledge gain and CFD validation per se. They are also essential for engineering such system of SITVC on aerospike nozzles for application and thrust vector controller design. Therefore, the engineer can either ensure a sonic injection by maintaining a p_{inj}/p_0-ratio above the threshold or adapt the controller to the complexer interdependencies with the main flow, when sub-sonic injection conditions occur.

DOI: 10.13009/EUCASS2023-435

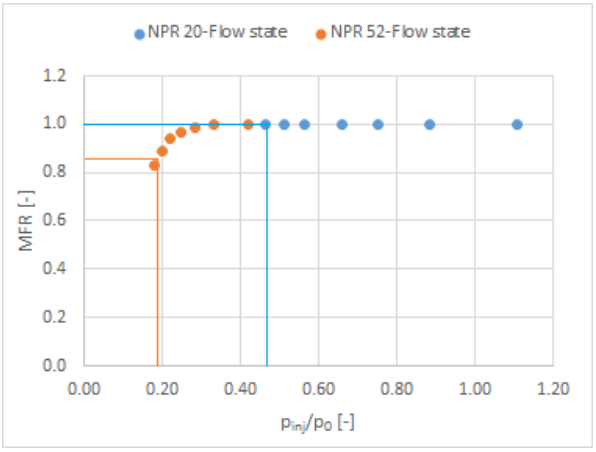

(a) Plug 2 ($x_{tr}/l_{is} = 64.5\,\%; x_{inj}/l_{is} = 40\,\%$)

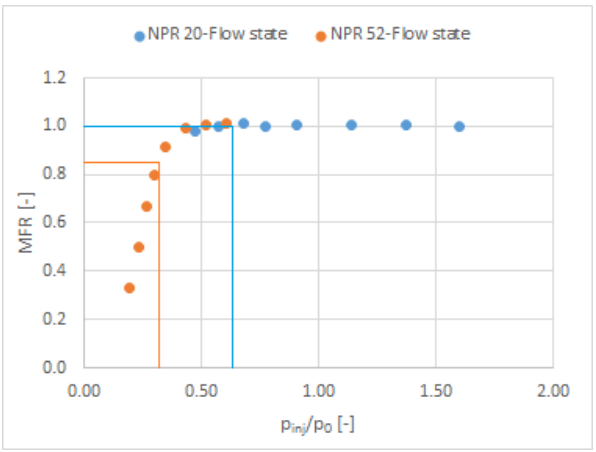

(b) Plug 3 ($x_{tr}/l_{is} = 64.5\,\%; x_{inj}/l_{is} = 15\,\%$)

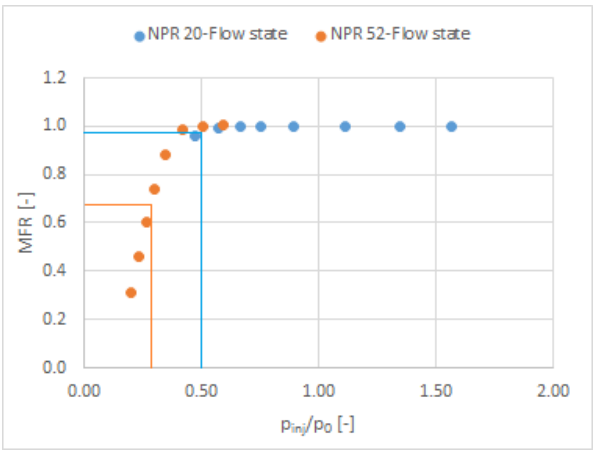

(c) Plug 4 ($x_{tr}/l_{is} = 34.5\,\%; x_{inj}/l_{is} = 15\,\%$)

Figure 14: Mass flow ratio-injection pressure ratio-correlation obtained in the vacuum wind tunnel test campaign

The latter is especially applicable, when the SITVC is not just on-off regulated e.g. by a fast opening and closing solenoid valve but rather with a continuously adjustable flow control valve.

5. Conclusion

A cold-gas test campaign with different linear aerospike nozzles and thrust-vector control through secondary injection has been conducted at the DLR test bench P6.2 in Lampoldshausen. The different nozzles were realized through exchangeable plugs - the super-sonic part of the aerospike nozzle - which enabled the investigation of two truncations and two injection positions. The goal of measuring the surface pressure along the nozzle wall and the nozzle base during different main flow states (over-expanded and under-expanded) with a secondary injection was achieved.

It could be shown, that a high pressure zone upstream and a low pressure zone downstream of the injection is present, which is in agreement with previous publications based on CFD analysis. Furthermore, it could be shown, that the combination of truncation and injection position have an interdependent influence on the base pressure and wake closure behaviour. A slight base pressure due to secondary injection could be observed for the plugs with less truncation ($x_{tr}/l_{is} = 64.5\,\%$) while for the one with higher truncation ($x_{tr}/l_{is} = 34.5\,\%$), no injection flow induced base pressure change could be detected. On the other hand, the further upstream injection position ($x_{inj}/l_{is} = 15\,\%$) showed a significant influence on the wake closing behaviour, reducing the critical nozzle pressure ratio at which the closure appears. For the downstream injection ($x_{inj}/l_{is} = 40\,\%$), no such influence could be observed. At last, the critical pressure ratio between the injecting and the primary flow was investigated in a follow-up campaign, revealing that the injection flow during the test campaign was in the trans-sonic regime.

DOI: 10.13009/EUCASS2023-435

In conclusion, the results of the presented test campaign provide a first insight into the surface pressure distribution on aerospike nozzles using secondary injection for thrust vector control. They show, that truncation and injection cause interdependent variations of the ideal isentropic expansion of the aerospike nozzle, which deserve further in-depth analysis. And at last, they can be used as a validation approach for the numerical simulation of comparable flow scenarios.

6. Acknowledgments

We appreciate the assistance and support by: The SAB (Sächsische Aufbaubank - Saxonian Development Bank) and the SMWK (Sächsisches Ministerium für Wissenschaft und Kunst - Saxonian Ministery for Science and Arts), who were funding the project ACTiVE (Ref.-Nr. 100323652); Dietmar Maier, test bench manager of cold gas test bench P6.2 in Lampoldshausen, who did always ensure a smooth test run. Furthermore, we would like to express our gratitude to our student Jonathan Bölk for his support in the data evaluation.

References

[1] G. Hagemann, H. Immich, and M. Terhardt. Flow phenomena in advanced rocket nozzles - the plug nozzle. *34th AIAA/ASME/SAE/ASEE Joint Propulsion Conference and Exhibit, Joint Propulsion Conferences*, July 1998.

[2] G. Hagemann, H. Immich, T. V. Nguyen, and G. E. Dumnov. Advanced rocket nozzles. *Journal of Propulsion and Power*, 14(5), September-Oktober 1998.

[3] M. Onofri, F. Nasuti, M. Calabro, G. Hagemann, H. Immich, P. Sacher, and P. Reijasse. Plug nozzles: Summary of flow features and engine performance. *AIAA*, (2002-0584), 2002.

[4] S. D. Eilers, M. D. Wilson, Dr. S. A. Whitmore, and Z. W. Perterson. Analytical and experimental evaluation of aerodynamic thrust vectoring on an aerospike nozzle. *AIAA*, (2010-6964), Juli 2010.

[5] E. Besnard and J. Garvey. Aerospike engine for nanosat and small launch vehicles (nlv/slv). Space 2004 Conference Exhibit, AIAA 2004-6005, September 2004.

[6] T. Bui, J. Murray, C. Rogers, S. Bartel, A. Cesaroni, and M. Dennett. Flight research of an aerospike nozzle using high power solid rockets. In *41st AIAA/ASME/SAE/ASEE Joint Propulsion Conference & Exhibit*. American Institute of Aeronautics and Astronautics (AIAA), 2005.

[7] J. Dennis, S. Shark, F. Hernandez, and J. K. Villarreal. Design of a n2o/htpb hybrid rocket motor utilizing a toroidal aerospike nozzle. In *48th AIAA Aerospace Sciences Meeting Including the New Horizons Forum and Aerospace Exposition*, 2010.

[8] AviationWeek. Firefly targets late fall for alpha aerospike rocket tests, 2016. http://aviationweek.com/space/firefly-targets-late-fall-alpha-aerospike-rocket-tests - Access date 15.12.2018.

[9] RocketStar. Welcome to rocketstar, 2017. http://rocketstar.nyc/ - Accessed 15.12.2018.

[10] Ripple Aerospace. Oceanic rocketry, 2017. https://rippleaerospace.com/ - Accessed 15.12.2018.

[11] Pangea Aerospace. Meso rocket, 2018. https://www.pangeaaerospace.com/meso-rocket/ - Accessed 07.07.2019.

[12] S. E. Group. Pangea aerospace successfullyhot fire tests the first methalox aerospike engine in the world. accessed Feb. 06, 2022.

[13] C. Bach, S. Schöngarth, B. Bust, M. Propst, J. Sieder-Katzmann, and M. Tajmar. How to steer an aerospike. In *69th International Astronautical Congress*, 2018.

[14] R. Silver. Advanced aerodynamic spike configurations - hot-firing investigations. Final Report AFRPL-TR-67-246-Vol II AD-384 856, Rocketdyne, September 1967.

[15] S. D. Eilers, M. D. Wilson, S. A. Whitmore, and Z. W. Peterson. Side-force amplification on an aerodynamic thrust-vectored aerospike nozzle. *Journal of Propulsion and Power*, 28:811–819, 2012.

[16] S. D. Eilers and S. A. Whitmore. Develompment and testing of a multiple use plug hybrid (for) nanosats (muphyn). In *26th Annual AIAA/USU Conference on Small atellites*, number SSC12-VI-3, 2012.

DOI: 10.13009/EUCASS2023-435

[17] S. D. Eilers, M. D. Wilson, and S. A. Whitmore. Design of a small scale aerospike nozzle and associated testing infrastructure for experimental evaluation of aerodynamic thrust vectoring. *Utah Space Grant Consortium - Session 2*, May 2010.

[18] M. Ferlauto, A. Ferrero, and R. Marsilio. Fluidic thrust vectoring for annular aerospike nozzle. In *AIAA Propulsion and Energy 2020 Forum*. American Institute of Aeronautics and Astronautics.

[19] M. Ferlauto, A. Ferrero, and R. Marsilio. Shock vector control technique for aerospike nozzles. In *AIAA Scitech 2020 Forum*. American Institute of Aeronautics and Astronautics.

[20] M. Ferlauto, A. Ferrero, M. Marsicovetere, and R. Marsilio. A comparison of different technologies for thrust vectoring in a linear aerospike. In *14th WCCM-ECCOMAS Congress*. CIMNE.

[21] M. Ferlauto, A. Ferrero, M. Marsicovetere, and R. Marsilio. Differential throttling and fluidic thrust vectoring in a linear aerospike. 6(2):8.

[22] M. Propst, J. Sieder, C. Bach, and M. Tajmar. Numerical analysis on an aerodynamically thrust-vectored aerospike nozzle. In *Proceedings of the 63rd German Aerospace Congress (DGLR), Augsburg*, 2014.

[23] M. Propst, V. Liebmann, J. Sieder-Katzmann, C. Bach, and M. Tajmar. Maximizing side force generation in aerospike nozzles for attitude and trajectory control. In *69th International Astronautical Congress*, 2018.

[24] J. Sieder, M. Propst, C. Bach, and M. Tajmar. Shallow water experiments to verify a numerical analysis on an aerodynamically thrust-vectored aerospike nozzle. In *Progress in Propulsion Physics – Volume 11*. EDP Sciences, 2019.

[25] M. Propst, L. Rümmler, S. General, V. Liebmann, J. Sieder-Katzmann, C. Bach, and M. Tajmar. Flow visualization and surface measurements of shallow water experiments exemplary for aerospike nozzles with secondary injection. In *Space Propulsion Conference*, 2018.

[26] J. Sieder-Katzmann, M. Propst, R. H. Stark, D. Schneider, S. General, M. Tajmar, and C. Bach. Active - experimental setup and first results of cold gas measurments for linear aerospike nozzles with secondary fluid injection for thrust vectoring. In *8th European Conference on Aeronautics and Aerospace Sciences (EUCASS)*, number 8.

[27] M. Frey, R. Stark, H. Cieaki, F. Quessard, and W. Kwan. Subscale nozzle testing at the p6.2 test stand. In *36th AIAA/ASME/SAE/ASEE Joint Propulsion Conference and Exhibit*. American Institute of Aeronautics and Astronautics, jul 2000.

[28] H. Kronmüller, K. Schäfer, H. Zimmermann, and R. Stark. Cold gas subscale test facility p6.2 at dlr lampoldshausen. In *6th International Symposium on Propulsion for Space Transportation of the XXI century, Palais des Congress, Versailles, France, 14 - 17 May 2002*, pages 1–8, 2002. LIDO-Berichtsjahr=2002,.

[29] K. Schäfer, C. Böhm, H. Kronmüller, R. Stark, and H. Zimmermann. P6.2 cold gas test facility for simulation of flight conditions - current activities. In *EUCASS 2005*, pages 1–7, 2005.

[30] G.-G. Börger. Optimierung von windkanaldüsen für den unterschallbereich [promotionsarbeit], 1973.

[31] G.-G. Börger. The optimization of wind-tunnel contractions for the subsonic range [ph. d. thesis], 1976.

[32] C. C. Lee. Technical note - fortran programs for plug nozzle design. Technical report, March 1963.

[33] M. Propst, J. Sieder-Katzmann, R. Stark, D. Schneider, S. General, M. Tajmar, and C. Bach. ACTiVE - Optimisation of a fluidic thrust vector control on aerospike nozzles. In *Space Propulsion Conference (SPC) 2021*.

[34] Jan Sieder-Katzmann, Martin Propst, Martin Tajmar, and Christian Bach. Cold gas experiments on linear thrust-vectored aerospike nozzles through secondary injection. In *70th International Astronautical Congress (IAC)*, number IAC-19-C4.10.8.x53736.

[35] J. Sieder-Katzmann, M. Propst, M. Tajmar, and C. Bach. Investigation of aerodynamic thrust-vector control for aerospike nozzles in cold-gas experiments. In *Space Propulsion* 2020 + 1, number *S PC*2020_406.